nature catalysis

ARTICLES

https://doi.org/10.1038/s41929-018-0195-1

Single platinum atoms immobilized on an MXene as an efficient catalyst for the hydrogen evolution reaction

Jinqiang Zhang[1,6], Yufei Zhao[1,6], Xin Guo[1], Chen Chen[2], Chung-Li Dong[3], Ru-Shi Liu[4], Chih-Pin Han[4], Yadong Li[2]*, Yury Gogotsi[5]* and Guoxiu Wang[1]*

Single-atom catalysts offer a pathway to cost-efficient catalysis using the minimal amount of precious metals. However, preparing and keeping them stable during operation remains a challenge. Here we report the synthesis of double transition metal MXene nanosheets—$Mo_2TiC_2T_x$, with abundant exposed basal planes and Mo vacancies in the outer layers—by electrochemical exfoliation, enabled by the interaction between protons and the surface functional groups of $Mo_2TiC_2T_x$. The as-formed Mo vacancies are used to immobilize single Pt atoms, enhancing the MXene's catalytic activity for the hydrogen evolution reaction. The developed catalyst exhibits a high catalytic ability with low overpotentials of 30 and 77 mV to achieve 10 and 100 mA cm^{-2} and a mass activity about 40 times greater than the commercial platinum-on-carbon catalyst. The strong covalent interactions between positively charged Pt single atoms and the MXene contribute to the exceptional catalytic performance and stability.

Hydrogen has been considered promising as a clean energy carrier to replace fossil fuels and can be produced by electrocatalytic water splitting[1–4]. Platinum is the most efficient catalyst for the hydrogen evolution reaction (HER)[5]. However, the scarcity and high cost of Pt severely hamper its widespread use in electrolysers for hydrogen production. Therefore, reducing the amount of Pt in the catalysts while maintaining high catalytic activity is essential for HER. In conventional Pt-based catalysts, not all Pt atoms are catalytically active due to the low utilization efficiency. Single-atom catalysts present an effective way to maximize the catalytic activity of Pt atoms, significantly reducing the amount of Pt to be loaded[6–14]. However, single Pt atoms tend to aggregate into nanoparticles during the synthetic and catalytic processes, leading to a decrease in catalytic activity[15]. Accordingly, it is critical to stabilize single Pt atoms on a conductive matrix to achieve optimized HER performance.

The strong covalent interactions between single atoms and such a matrix can efficiently anchor the individual atoms, avoiding the formation of aggregated particles. Most previously reported matrices have been composed of metals, metal oxides, metal carbides, metal sulfides and heteroatom- (for example, N) doped carbon materials, including Pt/FeO_x, Pt/α-Mo_2C, Co/MoS_2 and Ni(1)-NSG[8–10,13,16–22]. Single metal atoms trapped by defect sites in transition metal compounds form a unique class of single-atom catalysts. In particular, Pt, Pd or Au single atoms have been successfully trapped by defect sites in rod- or polyhedron-shaped ceria[6], Al_2O_3 (ref. [11]) and TiO_2 (ref. [23]). MXenes, a large family of emerging two-dimensional (2D) materials, have attracted tremendous attentions for applications in energy storage and conversion[24]. Owing to their superior metallic conductivity, chemical stability and hydrophilic properties, MXenes have been widely explored for electrical and magnetic shielding[25], lithium- and sodium-ion batteries[26,27], lithium–sulfur batteries[28], supercapacitors[29] and water splitting[30–33]. They have been used as catalyst supports[34–36], but only for large clusters and particles. While vacancies in the surface layer of MXenes have been reported[37,38], they have not yet been explored for anchoring single atoms through covalent bonding.

Herein, we report on the preparation of double transition metal MXene ($Mo_2TiC_2T_x$) nanosheets with abundant surface Mo vacancies (V_{Mo}) by electrochemical exfoliation ($Mo_2TiC_2T_x$–V_{Mo}), in which the Mo vacancies can act as the anchoring sites for single Pt atoms ($Mo_2TiC_2T_x$–Pt_{SA}). During the electrochemical exfoliation process, single Pt atoms are simultaneously immobilized on the Mo vacancies and are stabilized by the formation of covalent Pt–C bonds with the surrounding C atoms on the MXene. The resultant $Mo_2TiC_2T_x$–Pt_{SA} catalysts exhibit Pt-like kinetics towards the HER and show enhanced catalytic activity (30 and 77 mV at 10 and 100 mA cm^{-2}, respectively) with excellent stability (10,000 HER cycles or 100 h). In particular, the single Pt atom–MXene catalyst demonstrates a 39.5-fold increase in mass activity compared to the state-of-the-art commercial Pt/C catalyst. A population analysis from density functional theory (DFT) calculations suggests that the positively charged single Pt atoms supported on MXene comprise the optimum adsorption position for H^+, which facilitates hydrogen evolution.

Results

Synthesis and structural characterization of $Mo_2TiC_2T_x$–Pt_{SA}. $Mo_2TiC_2T_x$ MXene was prepared through HF etching of the quaternary transition metal carbides (MAX) phase (Mo_2TiAlC_2) by removing Al layers (Supplementary Figs. 1–8). Electrochemical exfoliation and in situ deposition were conducted by performing repeated

[1]Center for Clean Energy Technology, School of Mathematical and Physical Sciences, Faculty of Science, University of Technology Sydney, Sydney, New South Wales, Australia. [2]Department of Chemistry, Tsinghua University, Beijing, China. [3]Department of Physics, Tamkang University, Tamsui, Taiwan. [4]Department of Chemistry, National Taiwan University, Taipei, Taiwan. [5]A.J. Drexel Nanomaterials Institute and Department of Materials Science and Engineering, Drexel University, Philadelphia, PA, USA. [6]These authors contributed equally: Jinqiang Zhang and Yufei Zhao. *e-mail: ydli@mail.tsinghua.edu.cn; gogotsi@drexel.edu; guoxiu.wang@uts.edu.au

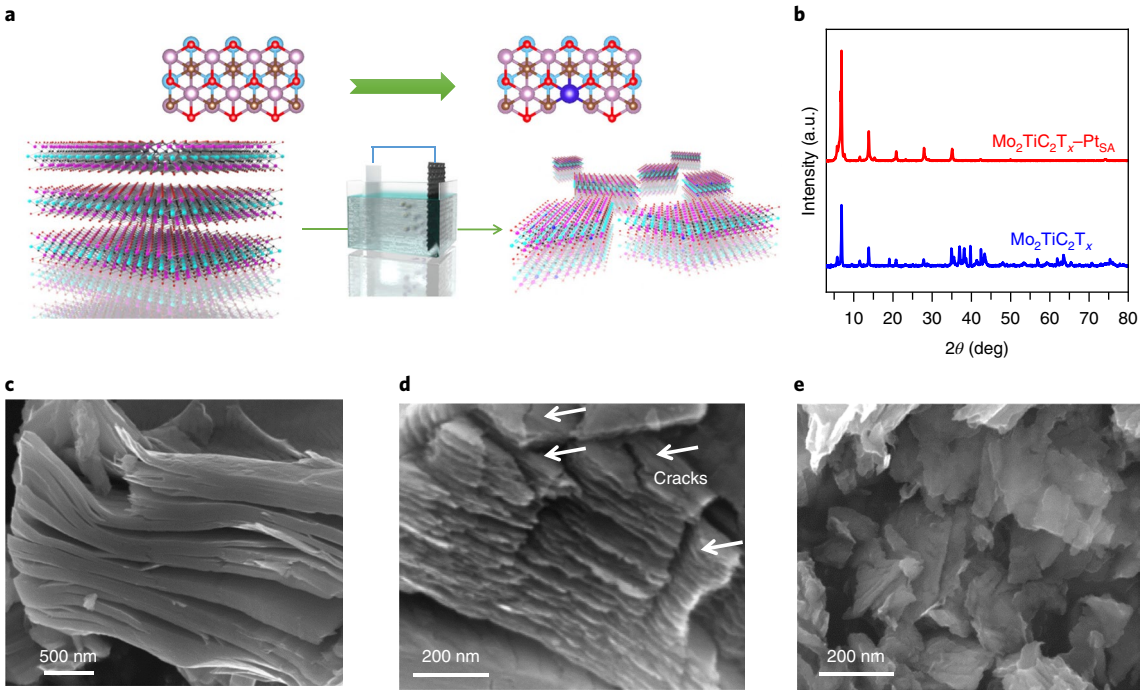

Fig. 1 | Morphology evolution of the catalysts during synthesis. a, Schematic of the electrochemical exfoliation process of MXene with immobilized single Pt atoms. **b**, XRD spectra of $Mo_2TiC_2T_x$ and $Mo_2TiC_2T_x$–Pt_{SA}. **c**–**e**, SEM images of MXene before (**c**), during (**d**) and after (**e**) the electrochemical exfoliation process.

linear sweep voltammetry scans using a three-electrode system with a Pt foil as the counter electrode and $Mo_2TiC_2T_x$ on carbon paper as the working electrode (Fig. 1a and Supplementary Fig. 9). During this process, the loosely packed $Mo_2TiC_2T_x$ was exfoliated into MXene nanosheets. Meanwhile, the Mo vacancies were created on the surface of MXene nanosheets and Pt atoms were simultaneously dissolved from the Pt foil counter electrode into the electrolyte and then trapped by the Mo vacancy sites. After 1,000 scanning cycles, Pt single atoms were immobilized on the exfoliated $Mo_2TiC_2T_x$ nanosheets, producing the desired catalyst ($Mo_2TiC_2T_x$–Pt_{SA}), while 1,500 electrochemical scan cycles led to the formation of Pt nanoparticles on the exfoliated MXene nanosheets ($Mo_2TiC_2T_x$–Pt_{NP}, confirmed in Supplementary Fig. 10), indicating the continuous in situ deposition of Pt atoms during the polarization scans. The X-ray diffraction (XRD) patterns in Fig. 1b shows that the dominant peaks of $Mo_2TiC_2T_x$–Pt_{SA} differ from those of the original MXene, but are identical to those of $Mo_2TiC_2T_x$ (delaminated using tetrabutylammonium hydroxide (TBAOH), Supplementary Fig. 11a). This demonstrates electrochemical exfoliation to 2D nanosheets. Furthermore, the XRD pattern of $Mo_2TiC_2T_x$–Pt_{SA} does not show the characteristic peaks of Pt, which also proves the absence of Pt nanoparticles in $Mo_2TiC_2T_x$–Pt_{SA}. Similarly, the Raman spectra in Supplementary Fig. 12 reveal the same peaks for $Mo_2TiC_2T_x$–Pt_{SA} and $Mo_2TiC_2T_x$ delaminated by TBAOH, further proving the exfoliation process. The morphology evolution of the MXene nanosheets is presented in Fig. 1c–e, where each image corresponds to a different stage during the HER scans. The loosely packed $Mo_2TiC_2T_x$ (Fig. 1c and Supplementary Fig. 13a) is gradually exfoliated, while the surfaces and edges curl up and crack in the first 300 cycles, as shown in the scanning electron microscopy (SEM) images in Fig. 1d and Supplementary Fig. 13b, eventually resulting in small pieces of MXene nanosheets after 1,000 cycles (Fig. 1e).

The transmission electron microscopy (TEM) and scanning transmission electron microscopy (STEM) images in Fig. 2a and Supplementary Fig. 14 further show that the exfoliated $Mo_2TiC_2T_x$ nanosheets consist of only a few layers of $Mo_2TiC_2T_x$. Bright spots are observed in the high-angle annular dark-field STEM (HAADF–STEM) image in Fig. 2b (circled), suggesting heavy constituent atoms in the structure, which confirms the formation of single Pt atoms on the MXene nanosheets. Furthermore, the magnified HAADF–STEM image in Fig. 2c shows that the Pt atoms are immobilized exactly at the Mo positions on $Mo_2TiC_2T_x$. We conducted a control experiment replacing the Pt foil counter electrode with a graphite rod to eliminate the deposition of Pt single atoms. A STEM image of the obtained MXene nanosheets after 1,000 cycles (Supplementary Fig. 15 and Supplementary Note 1) shows a large number of Mo vacancies on the basal plane ($Mo_2TiC_2T_x$–V_{Mo}). By comparing the STEM images of $Mo_2TiC_2T_x$–Pt_{SA} and $Mo_2TiC_2T_x$–V_{Mo}, we can conclude that the single Pt atoms are perfectly anchored to the sites of the Mo vacancies. We further performed STEM simulation on Pt-single-atom-immobilized $Mo_2TiC_2T_x$ based on the DFT-optimized structure (Fig. 2c). The simulated result is well consistent with the experimental STEM image. The energy-dispersive X-ray spectroscopy (EDS) analysis in Fig. 2d and Supplementary Fig. 16 shows that Pt atoms are well dispersed on ultrathin MXene nanosheets.

Electronic states of atoms in $Mo_2TiC_2T_x$–Pt_{SA}. We performed X-ray photoelectron spectroscopy (XPS), extended X-ray absorption fine structure spectroscopy (EXAFS) and X-ray absorption near-edge structure (XANES) measurements to further verify the presence and the electronic states of single Pt atoms immobilized on the $Mo_2TiC_2T_x$. The high-resolution XPS spectra in Supplementary Fig. 17 and Supplementary Note 2 show the reduced chemical states of Mo and Ti after the electrochemical exfoliation process. The high-resolution O 1*s* XPS peaks corresponding to Mo_2TiC_2–O_x, Mo_2TiC_2–OH and Mo_2TiC_2–OH_2 are enhanced, whereas the peaks for Mo–(Ti)–O from metal oxides become weaker after the electrochemical process. Moreover, the Pt 4*f* binding energies of $Mo_2TiC_2T_x$–Pt_{SA} are 75.6 and 72.0 eV, respectively, which shift to higher values compared

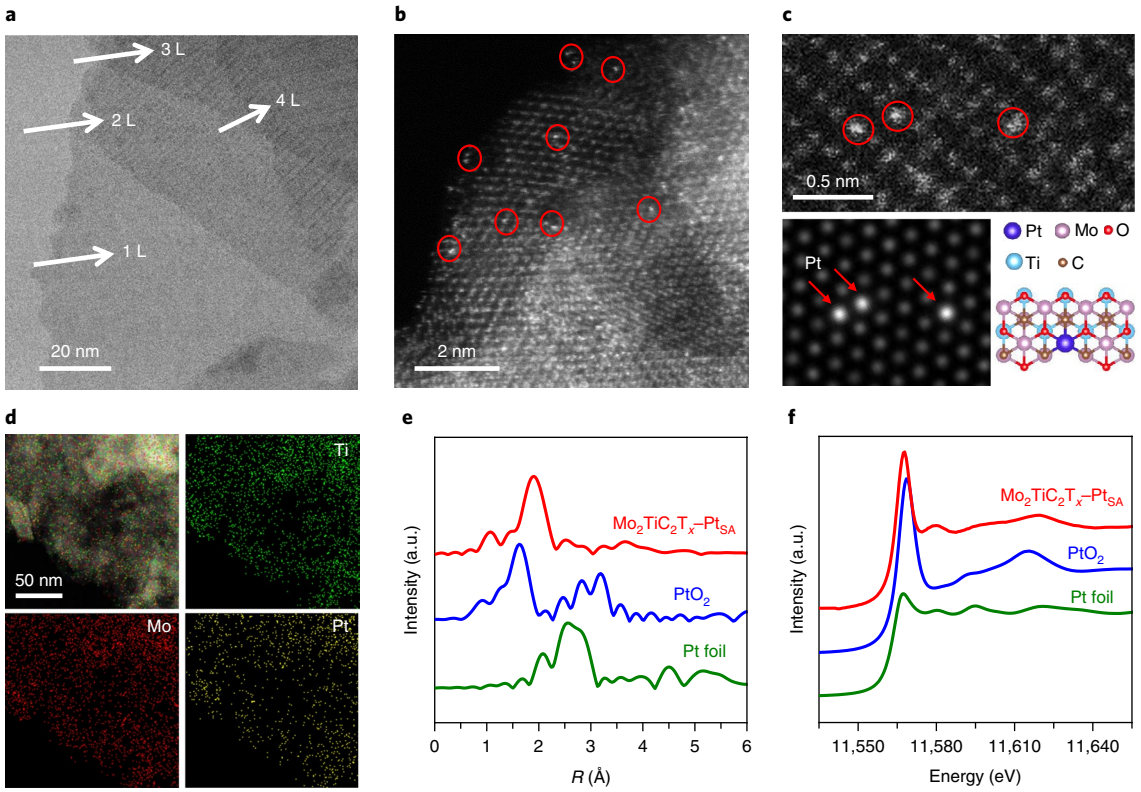

Fig. 2 | Structural characterization of the catalyst. a, TEM image of $Mo_2TiC_2T_x$-Pt_{SA}. **b**, HAADF-STEM image of $Mo_2TiC_2T_x$-Pt_{SA}. **c**, Magnified HAADF-STEM image of $Mo_2TiC_2T_x$-Pt_{SA} and its corresponding simulated image, and illustration of the structure of $Mo_2TiC_2T_x$-Pt_{SA}, showing the isolated Pt atoms (circles in **b** and **c**). **d**, STEM-EDS elemental mapping of $Mo_2TiC_2T_x$-Pt_{SA} nanosheets. **e**, The k^2-weighted Fourier transform of EXAFS spectra derived from EXAFS of Pt foil, PtO_2 and $Mo_2TiC_2T_x$-Pt_{SA}. *R* is the interatomic distance. **f**, Normalized XANES spectra at the Pt L_3-edge of Pt foil, PtO_2 and $Mo_2TiC_2T_x$-Pt_{SA}.

to commercial Pt/C (74.8 and 71.5 eV; Supplementary Fig. 17e). This indicates the formation of the oxidized Pt species[39,40]. The EXAFS results in Fig. 2e show Fourier transforms of the Pt L_3-edge EXAFS oscillations of the relevant materials (the k^2-weighted $\chi(k)$ signals in Supplementary Fig. 18), in which the Pt–Pt contribution at about 2.7 Å for Pt foil is absent for $Mo_2TiC_2T_x$–Pt_{SA}, strongly indicating that there are no Pt particles or clusters in the $Mo_2TiC_2T_x$–Pt_{SA}. Instead, the only prominent shell, located at 1.9 Å, mainly corresponds to Pt–C bonds[9]. The Fourier transform EXAFS curves and the fitting results are shown in Supplementary Fig. 19 and Supplementary Table 2. The fit gives a Pt–C coordination number for $Mo_2TiC_2T_x$–Pt_{SA} of 3, implying that single-atomic-site Pt coordinates with three C atoms on the MXene nanosheets. Based on the above analysis, each Pt atom is immobilized in the Mo vacancy and stabilized by forming three Pt–C bonds with the surrounding carbon. Moreover, two Pt–O bonds are also formed according to the fitted curve due to the overlapping orbitals of Pt and surrounding O-terminal atoms on the remaining Mo atoms, which is confirmed by comparing with the fitted curve with only three Pt–C (Supplementary Fig. 19b) and the mostly stabilized structure of the $Mo_2TiC_2T_x$–Pt_{SA}, as predicted by DFT calculations (Supplementary Table 3). XANES measurements were used to investigate the electronic state of the Pt species (Fig. 2f) and show that the intensity of $Mo_2TiC_2T_x$–Pt_{SA} is lower than that of PtO_2, but higher than that of the Pt foil. This proves that Pt single atoms in $Mo_2TiC_2T_x$–Pt_{SA} are positively charged (consistent with the XPS result), originating from Pt–C bonds and leading to electron transfer from the Pt to the $Mo_2TiC_2T_x$ nanosheets. All the above results unambiguously confirm that single Pt atoms have been successfully immobilized on the exfoliated $Mo_2TiC_2T_x$ nanosheets using the in situ electrochemical Pt deposition technique.

Mechanistic study on electrochemical exfoliation and Pt single-atom immobilization. We have proposed the mechanism of the electrochemical process (including exfoliation and the formation of Pt single atoms occupying the Mo vacancies) to be attributed to the facilitation of hydrogen cations (H^+) in acidic media alterating the surface chemical composition of the MXene (Fig. 3a). The O-terminated Mo_2TiC_2 ($Mo_2TiC_2O_2$) provides the active sites for hydrogen evolution[41,42]. Therefore, the basal planes with the O termination are capable of reducing water into hydrogen. H^+ initially interacts with the O-terminated Mo_2TiC_2 sites through hydrogen bonding, both on surface and edge sites. By receiving electrons from the conductive MXene, the H atom is grafted to a Mo–O terminal, leading to the formation of a Mo–OH intermediate (confirmed by XPS in Supplementary Fig. 17d). Further interactions between Mo–OH and H^+ can be divided into two possibilities. One is that the contact between H^+ and the active H atom from Mo–OH, with the aid of electrons from the substrate, resulting in hydrogen reduction and the formation of H_2 and restoration of the original Mo–O terminal (Heyrovsky process). The reversible reaction continuously generates H_2 gas both on the surface and between the MXene layers, which further delaminates MXene into a much looser structure (see SEM images in Fig. 1). The other possible route involves repeating interactions between the O atoms in Mo–OH and H^+ through hydrogen bonds. This process leads to the formation of a Mo–OH_2 intermediate (confirmed by XPS in Supplementary Fig. 17d). The existence of such an intermediate may result in the formation of either H_2 (Tafel process) or vacancies. The stronger Mo–O bond in Mo–OH_2 forces the breaking of C–Mo bonds, resulting in the formation of a Mo–OH_2 leaving group, its dissolution and the introduction of Mo vacancies on the surface of the MXene layer (see HAADF–STEM results in Supplementary Fig. 15)[43]. During H_2-assisted

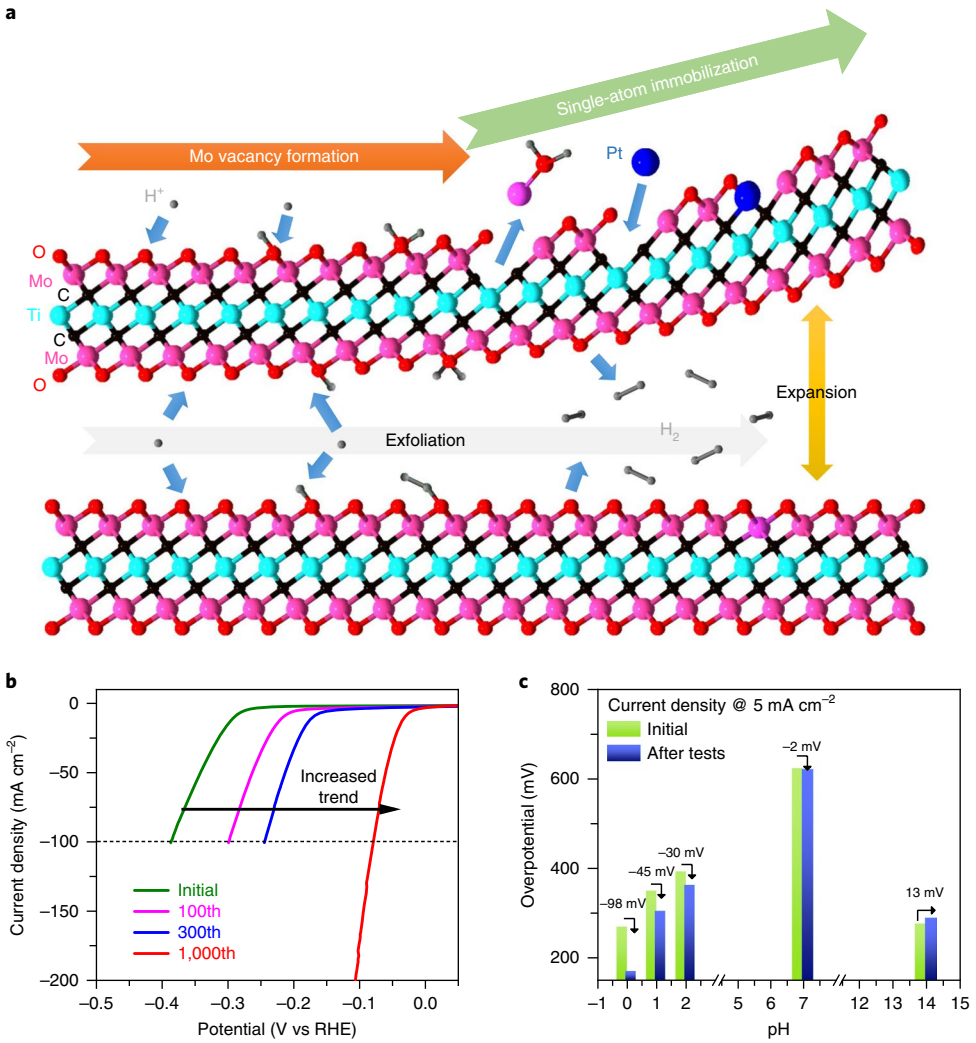

Fig. 3 | Investigation of the synthesis mechanisms of $Mo_2TiC_2T_x$–Pt_{SA}. **a**, Illustration of the synthesis mechanism for $Mo_2TiC_2O_2$–Pt_{SA} during the HER process. **b**, HER polarization curves of $Mo_2TiC_2T_x$ with Pt foil as the counter electrode, at different numbers of potential cycles. **c**, Overpotential change before and after testing (1,000 cycles) $Mo_2TiC_2T_x$ with a graphite rod instead of the Pt foil as the counter electrode at a current density of 5 mA cm^{-2} in solutions with different pH (0, 1, 2, 7 and 14 (100 cycles)).

delamination, the MXene layers are broken into small pieces (see SEM images in Fig. 1d,e) with accessible basal planes and defects, thus providing anchor sites for immobilization of Pt atoms and improving the HER performance. The HER catalytic performance of different cycles with Pt as counter electrode are shown in Fig. 3b, revealing the gradually enhanced catalytic current density and decreased overpotential. Proof experiments to identify the critical role of H^+ in the electrochemical exfoliation process were also conducted by testing the MXene in different pH solutions without Pt, and the results are summarized in Fig. 3c, Supplementary Figs. 20 and 21 and Supplementary Note 3. These results show that the HER catalytic performance is improved after 1,000 cycles in acid solution, suggesting that the exfoliation process indeed occurs with assistance from the electrochemical procedure. However, the enhancement in HER performance weakens with increasing pH (from 0 to 7) as the concentration of H^+ is reduced, correspondingly resulting in a lower efficiency of the delamination process facilitated by H^+ (Fig. 3c). Moreover, the HER performance decreases in alkaline media, probably due to MXene degradation or the interaction between K^+ and the negatively charged Mo–O terminals[44], deactivating the active sites of $Mo_2TiC_2T_x$ during long-time cycling (Supplementary Fig. 21c). However, direct use of acid-pre-treated $Mo_2TiC_2T_x$ ($Mo_2TiC_2T_x$–V_{Mo}) in neutral and alkaline solution shows a significant improvement in catalytic performance compared to the original $Mo_2TiC_2T_x$, further proving the electrochemical exfoliation process in acid solution (Supplementary Fig. 21b,d).

Electrochemical HER evaluation of $Mo_2TiC_2T_x$–Pt_{SA}. The HER activity of the $Mo_2TiC_2T_x$–Pt_{SA} was evaluated with the graphite rod as the counter electrode in 0.5 M H_2SO_4 solution. The original $Mo_2TiC_2T_x$, $Mo_2TiC_2T_x$–V_{Mo} and commercial Pt/C were also tested under the same condition. Interestingly, the electrochemically exfoliated $Mo_2TiC_2T_x$–V_{Mo} in Supplementary Fig. 22 shows better electrochemical HER performance than the organic solvent exfoliated $Mo_2TiC_2T_x$, demonstrating the superiority of the electrochemical exfoliation process. As shown in Fig. 4a, the $Mo_2TiC_2T_x$–Pt_{SA} shows the highest performance among all samples, requiring an overpotential of only 30, 77 and 104 mV to reach a current density of 10, 100 and 200 mA cm^{-2}, respectively, significantly better than the pristine $Mo_2TiC_2T_x$, the $Mo_2TiC_2T_x$–V_{Mo} and even the state-of-the-art commercial Pt/C catalyst at an overpotential of >65 mV. Additionally, the $Mo_2TiC_2T_x$–Pt_{SA} exhibits Pt-like kinetics with a

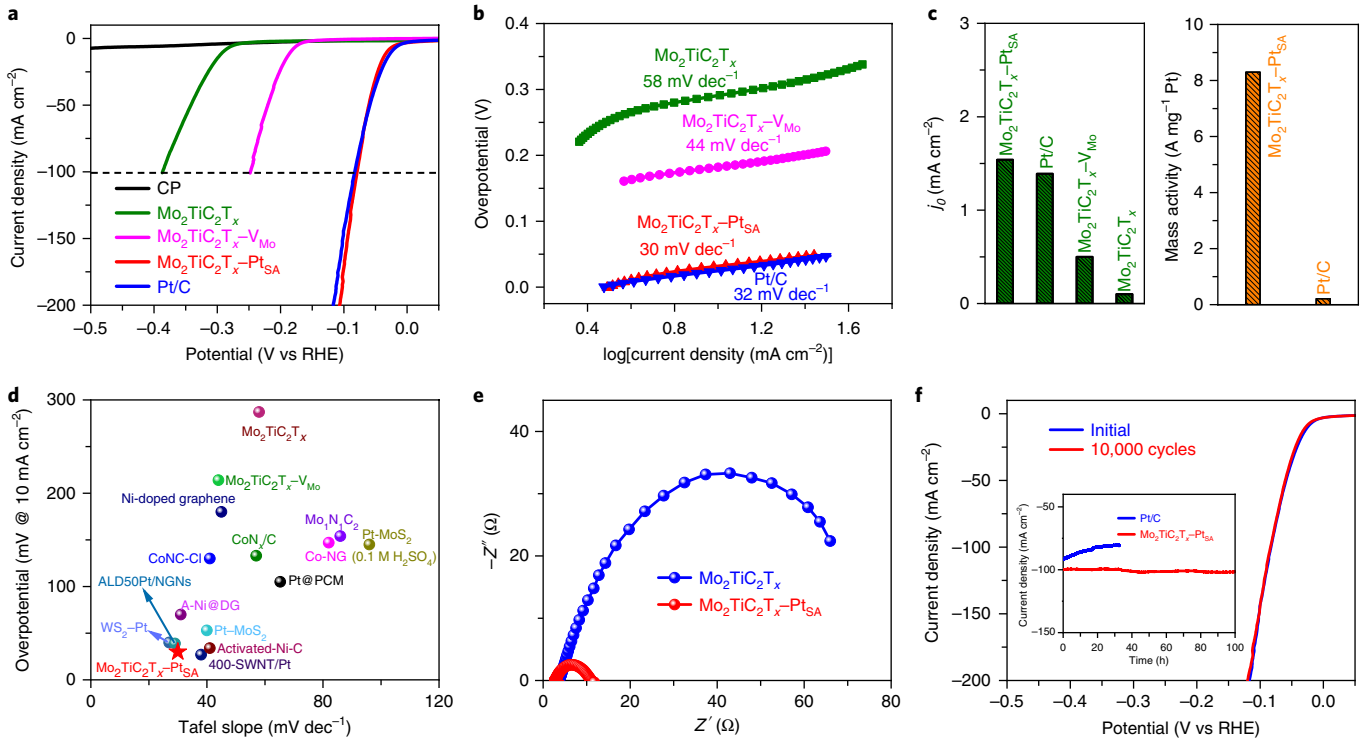

Fig. 4 | Electrocatalytic performance for $Mo_2TiC_2T_x$–Pt_{SA} and reference HER catalysts. a, HER polarization curves of carbon paper (CP), $Mo_2TiC_2T_x$, $Mo_2TiC_2T_x$–V_{Mo}, $Mo_2TiC_2T_x$–Pt_{SA} and Pt/C (40%), acquired using graphite rod as the counter electrode in 0.5 M H_2SO_4 solution. **b**, Corresponding Tafel slope derived from **a**. **c**, Exchange current densities of the catalysts, and the mass activity of state-of-the-art Pt/C and $Mo_2TiC_2T_x$–Pt_{SA}. **d**, Comparison of Tafel slope and overpotential (10 mA cm^{-2}) for various single-atom or Pt-based HER catalysts in 0.5 M H_2SO_4 solution. Values were plotted from references (Supplementary Table 4). **e**, EIS Nyquist plots of $Mo_2TiC_2T_x$–Pt_{SA} and $Mo_2TiC_2T_x$ catalysts. **f**, Stability test of $Mo_2TiC_2T_x$–Pt_{SA} through potential cycling, before and after 10,000 cycles. Inset: chronoamperometry curve of $Mo_2TiC_2T_x$–Pt_{SA} and Pt/C.

Tafel slope of 30 mV dec^{-1} towards HER (similar to the Tafel slope value of commercial Pt/C in Fig. 4b), revealing rapid HER kinetics derived from the advantage of introducing Pt single atoms. The $Mo_2TiC_2T_x$–Pt_{SA} delivers a fairly high exchange current density of 1.54 mA cm^{-2}, enhanced by factors of 15.4, 3.1 and 1.1 compared to pristine $Mo_2TiC_2T_x$, $Mo_2TiC_2T_x$–V_{Mo} and Pt/C, respectively (Fig. 4c). Furthermore, normalized to the Pt loading (1.2 wt%, inductively coupled plasma–mass spectrometry), the mass activity of HER for $Mo_2TiC_2T_x$–Pt_{SA} at an overpotential of 77 mV is 8.3 A mg^{-1}, which is 39.5 times greater than that of the commercial HER catalyst (40 wt% Pt/C, 0.21 A mg^{-1}). This result indicates that single Pt atoms immobilized on the MXene can maximize the catalytic activity, allowing significant cost reduction of the HER catalyst. The above merits of the $Mo_2TiC_2T_x$–Pt_{SA}, including low overpotential and Tafel slope, are superior to most previously reported single-atom or Pt-based HER catalysts (Fig. 4d and Supplementary Table 4). The isolated Pt single atoms trapped in the lattice defects of MXene even possess much higher catalytic activity than the aggregated Pt particles (the catalytic performance of $Mo_2TiC_2T_x$–Pt_{NP} shown in Supplementary Fig. 23), owing to the synergistic effect of the combination of Pt single atoms and the MXene host. Moreover, $Mo_2TiC_2T_x$–Pt_{SA} delivers excellent catalytic activity for HER in neutral solution (0.5 M PBS, 61 mV to achieve 10 mA cm^{-2}), exhibiting similar activity to Pt/C at an overpotential lower than 110 mV, whereas much higher current density is achieved at a more negative overpotential, demonstrating the efficient HER performance of $Mo_2TiC_2T_x$–Pt_{SA} in neutral electrolyte (Supplementary Fig. 24 and Note 4).

The electrochemically active surface area was first tested by performing cyclic voltammetry (CV) in the potential window between 0 and 0.5 V (versus reversible hydrogen electrode, RHE). Generally, the CV curves of trace Pt metal display characteristic redox peaks assigned to the adsorption/desorption of hydrogen. These features have been observed for commercial Pt/C[45,46], but are absent for the $Mo_2TiC_2T_x$–Pt_{SA} catalyst, suggesting the atomic catalysts have an ultralow amount of Pt (1.2 wt%) beyond the level of CV detection (for CV results see Supplementary Fig. 25a)[46]. The double-layer capacitance (C_{dl}) of the electrocatalyst was also measured to show the difference before and after exfoliation and Pt deposition[47]. The results (Supplementary Fig. 25b-d) illustrate that $Mo_2TiC_2T_x$–Pt_{SA} (68.1 mF cm^{-2}) exhibits a 7.02-fold increase in C_{dl} over $Mo_2TiC_2T_x$ (9.7 mF cm^{-2}), suggesting that the $Mo_2TiC_2T_x$–Pt_{SA} exposes more basal plane surface area, which is consistent with the SEM results in Fig. 1, thus providing more sites for the immobilization of Pt atoms and then enhancing HER performance. Moreover, the charge transfer resistance of the $Mo_2TiC_2T_x$–Pt_{SA} is much lower than that of $Mo_2TiC_2T_x$ (Fig. 4e), indicating a fast Faradaic process and superior HER kinetics for the $Mo_2TiC_2T_x$–Pt_{SA}, originating from the introduction of Pt single atoms.

Besides the aforementioned features, stability is another essential factor for real applications. We performed long-term stability tests for the $Mo_2TiC_2T_x$–Pt_{SA} catalyst, showing extremely high stability with no decay in HER performance for 10,000 cycles or 100 h (Fig. 4f). The characterizations, including EXAFS spectrum, HRSTEM image and electrochemical impedance spectra (EIS) Nyquist plots of $Mo_2TiC_2T_x$–Pt_{SA} after the stability test (Supplementary Fig. 26), indicate that the structure undergoes negligible changes, and no aggregation of single atoms is identified after long-term tests of hydrogen evolution, demonstrating the high stability of the single Pt atoms immobilized on the exfoliated $Mo_2TiC_2T_x$ nanosheets.

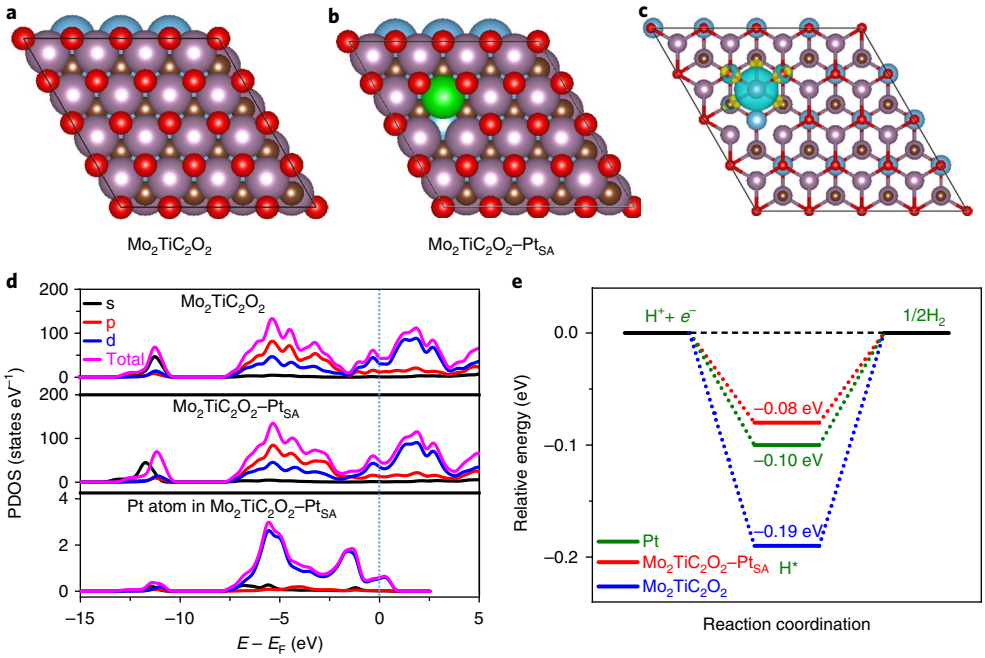

Fig. 5 | DFT calculation results. a,**b**, Top view of the slab models used to describe $Mo_2TiC_2O_2$ (**a**) and $Mo_2TiC_2O_2$-Pt_{SA} (**b**). Atoms in blue, purple, green, brown and red represent Ti, Mo, Pt, C and O, respectively. **c**, Calculated charge density distribution differences between $Mo_2TiC_2O_2$ and $Mo_2TiC_2O_2$-Pt_{SA}. The isosurface value is 0.01 e A^{-3} to better plot the differences. **d**, Calculated PDOS of $Mo_2TiC_2O_2$ and $Mo_2TiC_2O_2$-Pt_{SA}, with aligned Fermi level. **e**, Calculated free energy profiles of HER at the equilibrium potential for $Mo_2TiC_2O_2$, $Mo_2TiC_2O_2$-Pt_{SA} and Pt/C.

To further analyse the catalytic nature of $Mo_2TiC_2T_x$–Pt_{SA} towards HER, we incorporated thiocyanate ions (SCN^-), which are known to deactivate the metallic active sites under acidic conditions[47]. In Supplementary Fig. 27, the negligible HER deactivation for $Mo_2TiC_2T_x$ after the addition of SCN^- demonstrates that Mo–O sites instead of Mo atoms are the effective active sites. On the other hand, the significantly increased overpotential of the $Mo_2TiC_2T_x$–Pt_{SA} provides strong evidence that Pt single atoms are the effective HER sites.

DFT calculation of $Mo_2TiC_2O_2$–Pt_{SA} towards HER. We carried out DFT calculations to elucidate the catalytic contribution from Pt immobilization at $Mo_2TiC_2T_x$–Pt_{SA} for HER. The models for $Mo_2TiC_2O_2$ and $Mo_2TiC_2O_2$–Pt_{SA} were chosen (Fig. 5a,b) for the simulation. Based on the charge density distributions of $Mo_2TiC_2O_2$ and $Mo_2TiC_2O_2$–Pt_{SA} in Supplementary Fig. 28a,b, the replacement of a Mo atom by a Pt single atom causes a reduced charge density around the Pt atom, which is consistent with charge delocalizing from Pt to the surrounding atoms (supported by the charge density distribution differences in Fig. 5c). This suggests that incorporating single Pt atoms into the lattice of MXene could result in a redistribution of the electronic structure, which leads to an improved electron environment for catalysing the HER. Moreover, as illustrated by the projected density of states (PDOS) in Fig. 5d and Supplementary Fig. 29, the Pt-single-atom-immobilized MXene shows higher occupied states than the bare MXene near the Fermi level, which is associated with promoted electron transfer, leading to a higher conductivity of $Mo_2TiC_2O_2$–Pt_{SA}. The comparison between the PDOS of the $Mo_2TiC_2O_2$ and $Mo_2TiC_2O_2$–Pt_{SA} reveals that the enhanced DOS of the $Mo_2TiC_2O_2$–Pt_{SA} near the Fermi level is mainly contributed by the Pt *d* orbitals (Fig. 5d). This indicates that the individual single Pt atom can effectively improve the *d*-electron domination near the Fermi level, thus leading to enhanced catalytic activity. The work functions of $Mo_2TiC_2O_2$ and $Mo_2TiC_2O_2$–Pt_{SA} are shown in Supplementary Fig. 30 and Supplementary Note 5. The higher Fermi level and lower work function of $Mo_2TiC_2O_2$–Pt_{SA} indicate that $Mo_2TiC_2O_2$–Pt_{SA} has higher electronic energy levels and an improved capability to provide electrons. Therefore, it can be concluded that incorporation of Pt single atoms into the surface of MXene could further enhance the catalytic capability.

To further unravel the enhanced catalytic activity of $Mo_2TiC_2O_2$–Pt_{SA}, the free energy (ΔG_{H^*}) for hydrogen adsorption was investigated. Generally, there are three main steps for HER in acidic solution. The first step is the adsorption of protons on the active sites, H^+ reduction by e^-, followed by formation of the adsorbed intermediate H^*, and the final step is the release of molecular hydrogen. It is widely accepted that ΔG_{H^*} for hydrogen adsorption is a major descriptor for various HER catalysts. When the optimal value of ΔG_{H^*} is close to thermoneutral, that is $\Delta G_{H^*} \approx 0$, this suggests that the material is a good HER catalyst. As shown in Fig. 5e, ΔG_{H^*} of $Mo_2TiC_2O_2$ (on Mo–O terminal) is deduced to be −0.19 eV, validating strong hydrogen adsorption on Mo–O active sites. In contrast, the single Pt atom site on MXene is found to be a hydrogen generation active site for $Mo_2TiC_2O_2$–Pt_{SA} and the H^+ can adsorb at the single Pt site with a quite low adsorption energy of about −0.08 eV, which is even lower than for commercial Pt catalyst (−0.10 eV)[48]. The superior catalytic activity of $Mo_2TiC_2O_2$–Pt_{SA} for HER has demonstrated that the strength of hydrogen adsorption on the positively charged single-atom Pt on $Mo_2TiC_2O_2$–Pt_{SA} is less than on Pt atoms of the Pt/C catalyst, leading to faster formation and release of molecular hydrogen (Fig. 5e and Supplementary Fig. 31). It is worth noting that about thirty MXenes have already been reported and many more are possible[24]. They can be used as catalyst supports for single atoms of other metals, enabling and facilitating a number of catalytic processes.

Conclusions

In summary, an electrochemical exfoliation process has been developed to produce $Mo_2TiC_2T_x$ MXene nanosheets with abundant Mo vacancies, which offer active sites to trap single atoms and enhance

the catalytic performance of the MXene. The single Pt atoms immobilized on $Mo_2TiC_2T_x$ nanosheets exhibited Pt-like catalytic kinetics towards HER in acidic and neutral solutions, and the catalytic activity exceeded the most advanced commercial HER catalyst Pt/C, at a higher overpotential. Moreover, the $Mo_2TiC_2T_x$–Pt_{SA} shows excellent stability towards HER, due to the strong covalent bonding between Pt atoms and $Mo_2TiC_2T_x$, which prevents surface diffusion and coarsening of the catalyst. This work opens an alternative avenue for developing highly efficient single-atom catalysts supported on MXenes.

Methods

Synthesis of $Mo_2TiC_2T_x$ MXene. First, 1.0 g Mo_2TiAlC_2 powders were slowly added to an aqueous concentrated HF (45%) solution in a high-density polyethylene beaker. The suspension was constantly stirred for 48 h at 55 °C. The mixture was then washed and centrifuged by Ar de-aerated distilled water several times until the pH of the solution reached 6 to 7. The obtained suspension was freeze-dried at −49 °C for 24 h to eliminate the water in the solution.

Delamination of $Mo_2TiC_2T_x$ MXene using organic solvent. About 0.5 g of $Mo_2TiC_2T_x$ MXene powder was added to 10 ml of an aqueous solution of 54–56 wt% TBAOH ($((C_4H_9)_4NOH$), and the mixture was stirred for 24 h at room temperature. The resulting suspension was centrifuged and washed three times using Ar de-aerated deionized water to separate the intercalated powder from the TBAOH. After decantation of the supernatant, 40 ml of deionized water was added to the sediment and the mixture was sonicated for 1 h, before centrifuging for 1 h at 3,500 r.p.m. The supernatant was used for further characterization.

Synthesis of $Mo_2TiC_2T_x$–V_{Mo}. $Mo_2TiC_2T_x$–V_{Mo} was prepared using an electrochemical exfoliation process, which was performed in a three-electrode system. $Mo_2TiC_2T_x$ MXene deposited on a carbon paper electrode acted as the working electrode, and a graphite rod and a saturated calomel electrode (SCE) were used as the counter and reference electrodes, respectively. The in situ electrochemical exfoliation process was performed by repeating cathode polarization cycles in H_2SO_4 solution with a scan rate of 20 mV s^{-1} between 0 and −0.53 V versus RHE.

Synthesis of $Mo_2TiC_2T_x$–Pt_{SA}. $Mo_2TiC_2T_x$–Pt_{SA} catalyst was prepared using an in situ electrochemical exfoliation and atom trapping strategy, which was performed in a three-electrode system. $Mo_2TiC_2T_x$ MXene deposited on carbon paper acted as the working electrode, and Pt foil and an SCE were used as the counter and reference electrodes, respectively. The in situ electrochemical deposition process was performed by controlling cathode polarization cycles in 0.5 M H_2SO_4 solution with a scan rate of 20 mV s^{-1} between 0 and −0.6 V versus RHE.

Characterization. The morphology and chemical composition of the as-prepared samples were characterized by field-emission SEM (Zeiss Supra 55VP), EDS (Zeiss Evo SEM), TEM (Model JEM-2010, JEOL) and STEM (JEOL JEM-ARM200F). XRD measurements were conducted by employing a scanning step of 0.04° per second in the 2 θ range from 3 to 80° (Bruker D8 Discover XRD). XPS measurements were performed on an ESCALAB250Xi spectrometer (Thermo Scientific) equipped with mono-chromated Al Kα (energy 1,486.68 eV). Raman spectra were collected on an inVia Renishaw Raman spectrometer system (HR Micro Raman spectrometer, Horiba JOBIN YVON US/HR800 UV) using a 632.8 nm wavelength laser. Deposited Pt was measured by inductively coupled plasma–mass spectrometry on an Optima 7300 DV system (Perkin-Elmer Corporation). XANES and EXAFS measurements at the Pt L_3-edge were recorded in transition mode at beamline BL01C1 at the National Synchrotron Radiation Research Center (NSRRC), Taiwan. Pt foil and PtO_2 were used as reference samples. The carbon paper with $Mo_2TiC_2T_x$–Pt_{SA} was directly subjected to XANES and EXAFS measurements. Data analysis was carried out with Athena and Artemis in the Demeter package. Quantitative curve fittings were carried out in the k^2-weighted EXAFS oscillation in the range of 0–6 Å using the module ARTEMIS of IFEFFIT.

Electrochemical measurements. All electrochemical performance tests were carried out on an electrochemical workstation (CHI 660E, CH Instrument) using a three-electrode configuration with graphite rod as the counter electrode and an SCE as the reference electrode. The reference SCE was calibrated versus RHE, $E_{RHE} = E_{SCE} + 0.059 \times pH + 0.241$ V. The working electrode was carbon paper. To prepare the electrode slurry, 2 mg catalyst, 80 µl Nafion (5 wt%) and 1 ml ethanol were mixed and then sonicated for 30 min to form a dispersion. A 0.25 ml volume of the dispersion was dropped onto the carbon paper (area of 0.5 cm^2), followed by drying at room temperature in a vaccum oven. The typical catalyst loading was 1 mg cm^{-2}. Commercial Pt/C (40 wt%) catalyst powders were purchased from Johnson Matthey. For the purpose of consistency and ease of comparison, Pt/C electrode was prepared using the same amount of Pt/C with the same preparation procedure. A similar preparation procedure was used for $Mo_2TiC_2T_x$ samples using carbon paper as the working electrode, without Nafion, for characterization. Polarization curves were obtained in solutions with different pH (0, 1, 2, 7 and 14) at a scan rate of 5 mV s^{-1}, de-aerated with Ar at room temperature. CV measurements in the potential window 0–0.5 V (versus RHE) were performed for the $Mo_2TiC_2T_x$–Pt_{SA} sample. To measure the electrochemical capacitance of the catalysts, CV was conducted centred at the open-circuit potential at scan rates ranging from 10 to 100 mV s^{-1}. EIS spectra were recorded with a frequency ranging from 10^6 to 0.01 Hz and an amplitude of 5 mV at a certain potential. The cycling performance of the $Mo_2TiC_2T_x$–Pt_{SA} electrode was assessed by repeating linear sweep voltammetry for 10,000 cycles (scan rate of 20 mV s^{-1}), and current–time plots were obtained at a static overpotential.

DFT calculations. All geometry optimization and energy calculations were performed with DFT using the projector-augmented wave (PAW) method[49]. The generalized gradient approximation (GGA) functional of Perdew, Burke and Enzerhof (PBE) was used to analyse the exchange and correlation potential[50]. The local density approximate (LDA) functional of the Ceperley Alder parametrization of Perdew–Zunger (CAPZ) and the GGA function of the revised Perdew–Burke–Ernzerhof (RPBE) functional were also used for comparison. The semi-empirical London dispersion corrections of Grimme and colleagues[51] were conducted to calculate the interactions between absorbers and samples. The plane-wave cutoff energy level for all calculations was set as 400 eV, the self-consistent field (SCF) tolerance level was 2.0×10^{-5} a.u. for the geometry optimization and 1.0×10^{-6} a.u. for the energy calculation. The k space was sampled with a Γ point centred at 4×4×1 in geometry optimizations and at 6×6×1 in energy calculations for $Mo_2TiC_2O_2$ and $Mo_2TiC_2O_2$–Pt_{SA}, and at 2×2×1 in geometry optimizations and 4×4×1 in energy calculations for Pt.

The models of $Mo_2TiC_2O_2$ and $Mo_2TiC_2O_2$–Pt_{SA} with a 4×4×1 supercell were first chosen for simulation of the charge density distributions and the PDOS, while 3×3×1 and 4×4×1 supercell models of $Mo_2TiC_2O_2$–Pt_{SA} were chosen for the calculation of the work function.

For the adsorption calculation, 3×3×1 and 4×4×1 supercell models of $Mo_2TiC_2O_2$–Pt_{SA} were first calculated for the adsorption energy with an SCF tolerance level of 1.0×10^{-5} a.u. for comparison. As the adsorption energy difference between 3×3×1 and 4×4×1 supercell models was less than 0.001 eV, for further calculations we chose the model with a 3×3×1 supercell for $Mo_2TiC_2O_2$, with a 20 Å vacuum. The $Mo_2TiC_2O_2$–Pt_{SA} model was based on a geometrically optimized $Mo_2TiC_2O_2$ model, and a surface Mo atom was replaced by a Pt atom. Further free geometry optimizations and energy calculations were calculated based on the Mo_2TiC_2–Pt_{SA} model. For comparison, a Pt model achieved with a (111) surface in a modified 3×3×6 supercell (containing 216 Pt atoms) with 20 Å vacuum was used.

The free energy of the adsorbed state was calculated as follows based on the adsorption energy:

$$\Delta G_{H^*} = \Delta E_{H^*} + \Delta E_{ZPE} - T\Delta S$$

where ΔE_{H^*} is the adsorption energy of hydrogen and ΔE_{ZPE} is the difference corresponding to the zero point energy between the adsorbed state and the gas phase[48]. The adsorption site of hydrogen was confirmed by comparing the adsorption energy of hydrogen at different positions on the catalyst surface after free geometry optimizations with an SCF tolerance level of 5.0×10^{-5} a.u.

Data availability

The data that support the findings of this study are available from the corresponding authors upon reasonable request.

Received: 9 July 2018; Accepted: 18 October 2018;
Published online: 12 December 2018

References

1. Zou, X. & Zhang, Y. Noble metal-free hydrogen evolution catalysts for water splitting. *Chem. Soc. Rev.* **44**, 5148–5180 (2015).
2. Niether, C. et al. Improved water electrolysis using magnetic heating of FeC–Ni core–shell nanoparticles. *Nat. Energy* **3**, 476–483 (2018).
3. Liu, Y. et al. Self-optimizing, highly surface-active layered metal dichalcogenide catalysts for hydrogen evolution. *Nat. Energy* **2**, 17127 (2017).
4. Chen, C. et al. Highly crystalline multimetallic nanoframes with three-dimensional electrocatalytic surfaces. *Science* **343**, 1339–1343 (2014).
5. Morales-Guio, C. G., Stern, L.-A. & Hu, X. Nanostructured hydrotreating catalysts for electrochemical hydrogen evolution. *Chem. Soc. Rev.* **43**, 6555–6569 (2014).
6. Jones, J. et al. Thermally stable single-atom platinum-on-ceria catalysts via atom trapping. *Science* **353**, 150–154 (2016).
7. Cheng, N. et al. Platinum single-atom and cluster catalysis of the hydrogen evolution reaction. *Nat. Commun.* **7**, 13638 (2016).

8. Deng, J. et al. Triggering the electrocatalytic hydrogen evolution activity of the inert two-dimensional MoS_2 surface via single-atom metal doping. *Energy Environ. Sci.* **8**, 1594–1601 (2015).
9. Li, X. et al. Single-atom Pt as co-catalyst for enhanced photocatalytic H_2 evolution. *Adv. Mater.* **28**, 2427–2431 (2016).
10. Lin, L. et al. Low-temperature hydrogen production from water and methanol using Pt/α-MoC catalysts. *Nature* **544**, 80–83 (2017).
11. Zhang, Z. et al. Thermally stable single atom Pt/m-Al_2O_3 for selective hydrogenation and CO oxidation. *Nat. Commun.* **8**, 16100 (2017).
12. Zhang, L., Han, L., Liu, H., Liu, X. & Luo, J. Potential-cycling synthesis of single platinum atoms for efficient hydrogen evolution in neutral media. *Angew. Chem. Int. Ed.* **56**, 13694–13698 (2017).
13. Qiao, B. et al. Single-atom catalysis of CO oxidation using Pt_1/FeO_x. *Nat. Chem.* **3**, 634–641 (2011).
14. Li, H. et al. Synergetic interaction between neighbouring platinum monomers in CO_2 hydrogenation. *Nat. Nanotech.* **13**, 411–417 (2018).
15. Gao, C., Wang, J., Xu, H. & Xiong, Y. Coordination chemistry in the design of heterogeneous photocatalysts. *Chem. Soc. Rev.* **46**, 2799–2823 (2017).
16. Yang, H. B. et al. Atomically dispersed Ni(I) as the active site for electrochemical CO_2 reduction. *Nat. Energy* **3**, 140–147 (2018).
17. Liu, G. et al. MoS_2 monolayer catalyst doped with isolated Co atoms for the hydrodeoxygenation reaction. *Nat. Chem.* **9**, 810–816 (2017).
18. Fei, H. et al. General synthesis and definitive structural identification of MN_4C_4 single-atom catalysts with tunable electrocatalytic activities. *Nat. Catal.* **1**, 63–72 (2018).
19. Yang, X.-F. et al. Single-atom catalysts: a new frontier in heterogeneous catalysis. *Acc. Chem. Res.* **46**, 1740–1748 (2013).
20. Zhang, C. et al. Single-atomic ruthenium catalytic sites on nitrogen-doped graphene for oxygen reduction reaction in acidic medium. *ACS Nano* **11**, 6930–6941 (2017).
21. Yang, M. et al. Catalytically active Au-$O(OH)_x$-species stabilized by alkali ions on zeolites and mesoporous oxides. *Science* **346**, 1498–1501 (2014).
22. Liu, P. et al. Photochemical route for synthesizing atomically dispersed palladium catalysts. *Science* **352**, 797–800 (2016).
23. Wan, J. et al. Defect effects on TiO_2 nanosheets: stabilizing single atomic site Au and promoting catalytic properties. *Adv. Mater.* **30**, 1705369 (2018).
24. Anasori, B., Lukatskaya, M. R. & Gogotsi, Y. 2D metal carbides and nitrides (MXenes) for energy storage. *Nat. Rev. Mater.* **2**, 16098 (2017).
25. Shahzad, F. et al. Electromagnetic interference shielding with 2D transition metal carbides (MXenes). *Science* **353**, 1137–1140 (2016).
26. Naguib, M. et al. New two-dimensional niobium and vanadium carbides as promising materials for Li-ion batteries. *J. Am. Chem. Soc.* **135**, 15966–15969 (2013).
27. Xie, X. et al. Porous heterostructured MXene/carbon nanotube composite paper with high volumetric capacity for sodium-based energy storage devices. *Nano Energy* **26**, 513–523 (2016).
28. Liang, X., Garsuch, A. & Nazar, L. F. Sulfur cathodes based on conductive MXene nanosheets for high-performance lithium-sulfur batteries. *Angew. Chem. Int. Ed.* **54**, 3907–3911 (2015).
29. Lukatskaya, M. R. et al. Cation intercalation and high volumetric capacitance of two-dimensional titanium carbide. *Science* **341**, 1502–1505 (2013).
30. Ma, T. Y., Cao, J. L., Jaroniec, M. & Qiao, S. Z. Interacting carbon nitride and titanium carbide nanosheets for high-performance oxygen evolution. *Angew. Chem. Int. Ed.* **55**, 1138–1142 (2016).
31. Seh, Z. W. et al. Two-dimensional molybdenum carbide (MXene) as an efficient electrocatalyst for hydrogen evolution. *ACS Energy Lett.* **1**, 589–594 (2016).
32. An, X. et al. The synergetic effect of Ti_3C_2 MXene and Pt as co-catalysts for highly efficient photocatalytic hydrogen evolution over g-C_3N_4. *Phys. Chem. Chem. Phys.* **20**, 11405–11411 (2018).
33. Pandey, M. & Thygesen, K. S. Two-dimensional MXenes as catalysts for electrochemical hydrogen evolution: a computational screening study. *J. Phys. Chem. C* **121**, 13593–13598 (2017).
34. Satheeshkumar, E. et al. One-step solution processing of Ag, Au and Pd@ MXene hybrids for SERS. *Sci. Rep.* **6**, 32049 (2016).
35. Ming, M. et al. Promoted effect of alkalization on the catalytic performance of Rh/alk-$Ti_3C_2X_2$ (XO, F) for the hydrodechlorination of chlorophenols in base-free aqueous medium. *Appl. Catal. B* **210**, 462–469 (2017).
36. Li, Z. et al. Reactive metal–support interactions at moderate temperature in two-dimensional niobium-carbide-supported platinum catalysts. *Nat. Catal.* **1**, 349–355 (2018).
37. Karlsson, L. H., Birch, J., Halim, J., Barsoum, M. W. & Persson, P. O. Atomically resolved structural and chemical investigation of single MXene sheets. *Nano Lett.* **15**, 4955–4960 (2015).
38. Tao, Q. et al. Two-dimensional $Mo_{1.33}C$ MXene with divacancy ordering prepared from parent 3D laminate with in-plane chemical ordering. *Nat. Commun.* **8**, 14949 (2017).
39. Hunt, S. T., Milina, M., Wang, Z. & Román-Leshkov, Y. Activating earth-abundant electrocatalysts for efficient, low-cost hydrogen evolution/oxidation: sub-monolayer platinum coatings on titanium tungsten carbide nanoparticles. *Energy Environ. Sci.* **9**, 3290–3301 (2016).
40. Huang, X. et al. High-performance transition metal-doped Pt_3Ni octahedra for oxygen reduction reaction. *Science* **348**, 1230–1234 (2015).
41. Gao, G., O'Mullane, A. P. & Du, A. 2D MXenes: a new family of promising catalysts for the hydrogen evolution reaction. *ACS Catal.* **7**, 494–500 (2016).
42. Ling, C., Shi, L., Ouyang, Y. & Wang, J. Searching for highly active catalysts for hydrogen evolution reaction based on O-terminated MXenes through a simple descriptor. *Chem. Mater.* **28**, 9026–9032 (2016).
43. Liu, Y. et al. Low overpotential in vacancy-rich ultrathin $CoSe_2$ nanosheets for water oxidation. *J. Am. Chem. Soc.* **136**, 15670–15675 (2014).
44. Lian, P. et al. Alkalized Ti_3C_2 MXene nanoribbons with expanded interlayer spacing for high-capacity sodium and potassium ion batteries. *Nano Energy* **40**, 1–8 (2017).
45. Stamenkovic, V. R. et al. Improved oxygen reduction activity on $Pt_3Ni(111)$ via increased surface site availability. *Science* **315**, 493–497 (2007).
46. Tavakkoli, M. et al. Electrochemical activation of single-walled carbon nanotubes with pseudo-atomic-scale platinum for the hydrogen evolution reaction. *ACS Catal.* **7**, 3121–3130 (2017).
47. Zhang, H. et al. Dynamic traction of lattice-confined platinum atoms into mesoporous carbon matrix for hydrogen evolution reaction. *Sci. Adv.* **4**, eaao6657 (2018).
48. Nørskov, J. K. et al. Trends in the exchange current for hydrogen evolution. *J. Electrochem. Soc.* **152**, J23–J26 (2005).
49. Blöchl, P. E. Projector augmented-wave method. *Phys. Rev. B* **50**, 17953 (1994).
50. Perdew, J. P. Density-functional approximation for the correlation energy of the inhomogeneous electron gas. *Phys. Rev. B* **33**, 8822 (1986).
51. Grimme, S. Semiempirical GGA-type density functional constructed with a long-range dispersion correction. *J. Comput. Chem.* **27**, 1787–1799 (2006).

Acknowledgements

The authors thank P. Li from Nanjing University of Aeronautics and Astronautics, Nanjing for performing DFT calculations. Y. Zheng from the University of Adelaide and Y.-C. Huang from the National Synchrotron Radiation Research Centre are acknowledged for their valuable discussions. The authors acknowledge use of the JEOL 2010 and JEOL JEM-ARM200F STEM within the University of Wollongong (UoW) Electron Microscopy Centre. This project was financially supported by the Australian Research Council (ARC) through ARC Discovery projects (DP160104340 and DP170100436) and a Rail Manufacturing CRC (RMCRC) project.

Author contributions

G.W., J.Z. and Y.Z. conceived the idea. J.Z. and Y.Z. performed the electrochemical experiments. X.G. synthesized the $Mo_2TiC_2T_x$ MXene. Y.G. provided the MAX materials for this work. J.Z., Y.Z. and X.G. carried out characterizations. C.-L.D., R.-S.L. and C.-P.H. performed and analysed EXAFS and XANES analysis. J.Z., Y.Z., C.C., Y.L., Y.G. and G.W. proposed the mechanism research and discussions. All authors contributed to writing of the manuscript.

Competing interests

The authors declare no competing interests.

Additional information

Supplementary information is available for this paper at https://doi.org/10.1038/s41929-018-0195-1.

Reprints and permissions information is available at www.nature.com/reprints.

Correspondence and requests for materials should be addressed to Y.L. or Y.G. or G.W.

Publisher's note: Springer Nature remains neutral with regard to jurisdictional claims in published maps and institutional affiliations.